Materials Advances

Accepted Manuscript

This article can be cited before page numbers have been issued, to do this please use: P. Mukherjee, Y. Cho, P. Panitha and T. Taniike, *Mater. Adv.*, 2025, DOI: 10.1039/D5MA00345H.

ROYAL SOCIETY OF CHEMISTRY

rsc.li/materials-advances

View Article Online
DOI: 10.1039/D5MA00345H

ARTICLE

Accelerated Perovskite Discovery: Screening New Catalysts for Photocatalytic Methylene Blue Degradation

Received 00th January 20xx,
Accepted 00th January 20xx

DOI: 10.1039/x0xx00000x

Poulami Mukherjee,* Yohei Cho, Panitha Phulkerd, and Toshiaki Taniike*

The diversified use of metal oxides within several disciplines underlines their flexibility in various catalytic processes and innovations in material science. Multimetallic oxides, because of tailored functionality, improved stability, and enhanced conductivity, offer a wider range of applications compared to single-metal counterparts. Among them, perovskites stand out, being a class suitable for various applications, including photocatalysis. One among them is the photocatalytic degradation of methylene blue (MB), a process increasingly recognized for its importance in environmental remediation and water purification. Herein, we present a simple, economical, and easily adaptable high-throughput experimentation approach to synthesize and evaluate a wide array of citric acid-assisted perovskite compositions for photocatalytic degradation. Our high-throughput approach not only addresses the bottleneck of catalyst preparation but also expands the scope of photocatalysis research by incorporating computational screening of less-explored perovskite compositions. The obtained data will serve as valuable references for the development of next-generation catalysts, as we have drawn a correlation between material property and their performance. Moreover, the synthetic methodology, if adopted, permits the synthesis of any kind of metal oxides for applications ranging from homogeneous to heterogeneous catalysis and further into broader domains of materials science.

Keywords: High-throughput, Perovskites, Citric acid, Methylene Blue, Photocatalysis

1. Introduction

Robust-performance metal oxides represent one of the most versatile classes of materials in modern science, owing to the possibilities of tailoring their structural, electronic, and chemical properties in ways that make them critical in various fields ranging from environmental catalysis to energy conversion and storage.[1–3] Having the feasibility of leveraging additional metals with varying properties, multi-metal oxides offer a wider range of functions with improved performances, stability, and enhanced conductivity compared to single-metal-based oxides.[4,5] Among them, perovskite constitutes that special class of metal oxide which is particularly striking due to its adaptability and finds vital applications across scientific disciplines.[2,5,6]

Amidst the major applications of perovskite materials, photocatalysis has a greater drive toward encouraging energy efficiency in chemical reactions in a sustainable manner.[7–10] The degradation of the environmental pollutant methylene blue (MB), a common cationic dye used within many industries, has been one of the main areas of focus in photocatalysis.[11,12] MB is a non-biodegradable compound and has become an important environmental pollutant, especially in water ecosystems.[13] The increased application of the compound has necessitated the development of effective and sustainable methods for removing MB from wastewater.[14,15] Conventional methods such as adsorption,[16,17] coagulation,[18] and biological treatments[19] often lead to incomplete degradation, accompanied by drawbacks such as high operational costs and the generation of secondary pollutants. In this aspect, advanced oxidation processes are especially appealing because, using sunlight as an activator of photocatalysts, they allow organic dyes to be completely mineralized into environmentally benign end products such as CO_2 and H_2O.[20–24]

Perovskite materials have a unique ability to incorporate a wide range of elements and provide enhanced tunability in band positions, charge carrier mobility, and other electronic properties.[2,7] Such wide composition flexibility in the case of an ABO_3 perovskite structure is enabled by the possibility of varying both A- and B-site cations within a tolerance factor of approximately 0.8-1.0.[25] In fact, it is certain that each variation can significantly impact the photocatalytic efficiency of the material. Thus, systematic screening of a large number of material compositions under various conditions is essential to exploring a vast parameter space efficiently and identifying optimal combinations that maximize MB degradation. In this prospect, making the synthesis and evaluation at comparable throughput is of utmost importance. By scaling up material exploration, new high-performance materials that conventional trial-and-error approaches might not have explored could be

Graduate School of Advanced Science and Technology, Japan Advanced Institute of Science and Technology, 1-1 Asahidai, Nomi, Ishikawa, 923-1292, Japan.
** Corresponding authors*

† Supplementary Information available: [details of any supplementary information available should be included here]. See DOI: 10.1039/x0xx00000x

View Article Online DOI: 10.1039/D5MA00345H

discovered, thereby advancing the development of more effective and sustainable photocatalytic solutions. To achieve this, an approach mandating high-throughput experimentation (HTE) in both catalyst preparation and performance evaluation will be required.[26–29] While the term HTE may initially sound a little overwhelming for material researchers, complexity in synthesis and evaluation processes is inevitable because humans lack efficiency in managing and analyzing a huge array of variables that cover material compositions, processing conditions, and performance metrics. Needless to say, the real bottleneck in such catalysis research lies in the labor-intensive preparation methods for the catalysts.

Among the different synthesis methodologies, the citric acid-assisted synthesis of metal oxides, including perovskites, has several notable advantages compared to the conventionally applied techniques of combustion, solid-state reactions, hydrothermal synthesis, co-precipitation, and classical sol-gel processes.[30,31] In metal oxide synthesis, citric acid (CA), as a complexing agent, can stabilize the metal ions, preventing their premature precipitation. It also accelerates gelation, promoting the formation of a homogeneous precursor gel.[32,33] The two characteristics are very important in the case of ternary or quaternary metal oxide formations, where the CA matrix inhibits the phase segregation during the synthesis, ensuring a single-phase product without impurities. Typically, ionic nitrate salts are preferred in this process since they usually tend to be stronger oxidizers compared to pure oxygen. Together with organic citrate salts, they undergo a low-temperature oxidation-reduction reaction and self-ignite. Finally, the process is relatively simple and can be easily scaled up for industrial applications.

In light of all these merits, this study tackles the challenges of HTE by designing a parallelizable synthetic route for CA-assisted perovskite materials and screening their photocatalytic activity for MB degradation. The study highlights the role of CA in perovskite synthesis by comparing selected samples prepared with and without CA. By analyzing the morphological difference among these samples, we demonstrate how CA influences principal synthesis parameters like nucleation and particle dispersion and acts as a structure-directing agent to form either well-dispersed nanoparticles or an ordered framework, depending on the elemental composition. Besides the perovskite synthesis for MB degradation, the wide applicability of high-throughput synthesis approaches extends to synthesizing any mixed oxides that might find applications in catalysis, energy storage, sensors, and environmental protection, among many others. The scope of the study includes perovskites that are not commonly studied for photocatalysis, yet show potential for effective MB degradation, as filtered by a computational database based on several key factors. Results obtained from this paper will guide the readers not only to parallelizable synthetic techniques, which allow rapid synthesis of many catalysts within a short time frame, but also to the fact that the photocatalytic screening results were obtained under unified conditions, will allow researchers to observe trends, correlations, and design principles for future material exploration using the synthesized perovskites as valuable reference data. We have also explained their photocatalytic performance in terms of multiple physical properties like formation energy, bandgap, etc.

2. Experimental Method

2.1 Material selection

17 candidates are selected for the photocatalytic degradation of MB from the Materials Project database[34,35] for photocatalytic degradation of MB based on the following criteria:

1. Material includes the original 23 elemental selection. Elements whose oxides are widely employed in heterogeneous reactions, especially redox catalysis, are focused. Certain elements, namely molybdenum (Mo) and chromium (Cr), are intentionally excluded due to sublimation risks and safety issues. **Table S1** lists the chosen elements with their precursor salts.

2. Energy_abole_hull (parameters relating to stability) =0, and the materials are listed in ICSD. The energy above the hull measures the thermodynamic stability of a given material.[34] If the energy value is 0 eV, it means that the material lies on the convex hull of stability, which, physically, means that it will not spontaneously decompose into other phases since this is the most stable phase. This is a critical parameter in the first-level screening of a material's synthesizability, with the consideration that photocatalysts must withstand the conditions of the reaction without degrading or being converted into less active phases. To further ensure synthesizability, those combinations listed in the Inorganic Crystal Structure Database (ICSD) are preferred, allowing us to claim success for our high-throughput synthesis method.

3. Chemical formula represented in ABO_3 form. A and B are elements selected based on criterion 1, and O corresponds to oxygen. For the broad-range applicability of perovskite materials, the synthesis of perovskite structures is intended by the parallel approach.

4. Bandgap within the range of 0.5-4.0 eV. A bandgap in this range is necessary for both absorbing sufficient sunlight to generate electron-hole pairs and having the overpotential needed to drive photocatalytic reactions. A too-small bandgap is inappropriate as they do not satisfy the thermodynamic criteria for conduction/valence band edge positions higher/lower than the redox potential, respectively, and cannot drive photocatalytic reactions. Conversely, a bandgap that is too large cannot absorb optimal sunlight to generate an electron-hole pair and will not drive the reaction. It should be noted that the calculated bandgap is usually underestimated compared to the experimentally obtained value, but to cover the large variety, a wider range than the sunlight is set.

Table S2 displays the list of the 17 candidates chosen for perovskite synthesis.

2.2 High-throughput synthesis of perovskite materials

View Article Online
DOI: 10.1039/D5MA00345H

Here, the synthesis procedure of 17 perovskites is demonstrated in parallel. At first, 16 precursor solutions were prepared by dissolving individual metal nitrate salts in 20 mL of deionized (DI) water. The solutions were stirred with a multi-stirrer for 30 minutes for homogeneity. Next, 20 mL of CA was added to each of the 16 solutions in a molar ratio of 0.5:1.0 metal: CA and stirred at 60 °C for an additional 30 minutes to make the stock solutions. The solutions thus formed were stored in the refrigerator.

It is important to note that for the titanium precursor, titanium tetrabutoxide [$Ti(OCH_2CH_2CH_2CH_3)_4$] was used, which was freshly prepared by dissolving it in absolute ethanol. Additionally, the CA solution was also prepared in absolute ethanol. Both preparation steps were conducted under an inert atmosphere to prevent unwanted reactions. All other conditions were maintained consistently, as previously described.

Figure 1: Schematic illustration of the catalyst synthesis process with pictorial representation.

To prepare the final reaction solutions, 10 mL of the desired individual metal stock solution was added to make the total volume of 20 mL for each mixture, Figure 1(a). These solutions were then evaporated at 100°C under continuous stirring conditions, Figure 1(b). After 4-5 hours, the formed gels, Figure 1(c), were transferred into crucibles while still warm and less viscous. They were then set to dry in a muffle furnace at 120 °C for 12 hours. The semi-solidified gels were crushed to break any foaming caused during the degassing process. The crushed products obtained were subsequently calcined in a muffle furnace, first at 350 °C and then at 1000 °C, with a controlled heating rate of 2 °C per minute, Figure 1(d). Afterward, the final products were milled to produce fine perovskite powders, Figure 1(e). To investigate the role of CA in metal oxide synthesis, a few metal oxides, namely $CaTiO_3$, $SrTiO_3$, $MgTiO_3$, and $CaZrO_3$, were also prepared without CA, following the same procedure except for the addition of CA. These perovskites were specifically selected based on their photocatalytic performance: $CaTiO_3$ exhibited the highest activity, while $MgTiO_3$ showed the lowest. $SrTiO_3$ was included as it is one of the most widely studied perovskites, and $CaZrO_3$ demonstrated intermediate activity.

2.3 Material Characterizations

The XRD patterns were recorded in the 2θ range of 3–90° at a speed of 10°/min and a step size of 0.01° on MiniFlexC600 (Rigaku) with Cu Kα radiation (λ = 1.5418 Å). The morphologies of the as-synthesized perovskites were examined using TEM with H-7650 (Hitachi, Tokyo, Japan) at an acceleration voltage of 100 kV. The samples were dispersed in ethanol with ultrasonication for 15 min, then dropped onto a carbon-coated copper grid and naturally dried overnight. N_2 adsorption/desorption experiments were performed on a BELSORP Mini (BEL Japan, Tokyo, Japan) instrument at 77 K. An amount of 80–100 mg of catalyst was loaded into a glass cell, followed by degassing performed under vacuum at 150°C for 2h before the measurement.

2.4 High-throughput photocatalyst screening

A Xenon (Xe) lamp with a light spectrum proximate to sunlight was employed, delivering an intensity of 250 W/m². The reaction was carried out at a practical condition of 20 °C. The MB concentration was fixed at 6.6 ppm to ensure adequate sensitivity for its detection. Each perovskite sample included in Table 1 was used in the reaction at 100 µg. After adsorption for 1 hour, we monitored the samples in the dark for another hour to evaluate their dark performance. Then, the samples were exposed to light for 3 hours; absorbance was measured every 15 minutes to monitor the degradation of MB. Each experiment was performed three times to ensure the reliability of the data (N=3). The reaction was performed using a parallelized approach to efficiently manage the screening process. To evaluate the photocatalytic performance, the absorbance at the characteristic wavelength of 665 nm (OD_{665}) was monitored, while the background absorbance at 800 nm (OD_{800}) was simultaneously recorded. The effective absorbance was defined as $\Delta OD = OD_{665} - OD_{800}$. The reaction rate constant (k) was determined by performing a linear regression on the decay of ΔOD over time. The rate constant was then converted to account for the calibration coefficient (expressed in ppm per unit OD), the reaction volume, and the mass of the perovskite catalyst, according to Eq. 1

$$k = -\frac{\mathrm{d}}{\mathrm{d}t}(OD_{665} - OD_{800}) \times (\text{conversion coefficient}) \times \frac{solution\ volume}{perovskite\ mass} \qquad Eq.\ 1$$

3. Results and Discussion

3.1 Characterization of Synthesized Materials

Powder X-ray diffraction (PXRD) spectroscopy confirmed the successful synthesis of 16 perovskites. The diffraction patterns of each sample were matched with their corresponding Joint Committee on Powder Diffraction Standards (JCPDS) reference number, Table 1, to confirm the correct phase and crystallinity of the material. All the perovskites show well-developed diffraction peaks, suggesting a relatively large domain size. This is reasonable due to the high calcination temperature used to produce them. The XRD patterns of the 17 combinations are shown in Figure S1.

View Article Online
DOI: 10.1039/D5MA00745H

Table 1: Confirmation of product formation with their corresponding phases.

No.	Combination	JCPDS	Crystal structure
1.	$NdFeO_3$	00-025-1149	monoclinic
2.	$BaZrO_3$	00-006-0399	cubic
3.	$PrFeO_3$	00-019-1012	orthorhombic
4.	$BaTiO_3$	01-075-2116	tetragonal
5.	$CaTiO_3$	01-075-2100	cubic
6.	$LaInO_3$	00-008-0148	undefined
7.	Pr_2O_3, In_2O_3	00-047-1111, 01-088-2160	hexagonal, cubic
8.	$LaFeO_3$	00-015-0148	orthorhombic
9.	$BaNiO_3$	01-070-0108	hexagonal
10.	$MgTiO_3$	00-006-0494	rhombohedral
11.	$CaZrO_3$	00-035-0645	orthogonal
12.	$InGaO_3$	01-075-0975	hexagonal
13.	$BaCeO_3$	00-022-0074	orthorhombic
14.	$SrZrO_3$	01-074-2231	cubic
15.	$LaCoO_3$	00-048-0123	rhombohedral
16.	$LaAlO_3$	01-085-0848	rhombohedral
17.	$SrTiO_3$	01-074-1296	cubic

Note: In the efforts to synthesize 17 perovskites using the CA method, the successful synthesis of 16 perovskites was confirmed; the expected $PrInO_3$ was not formed. Instead, a mixed oxide phase consisting of Pr_2O_3 and In_2O_3 was observed. One possible reason for this unsuccessful synthesis may be that the reaction conditions, such as temperature and time, might not have been optimal for this ternary oxide. The reaction conditions may stabilize mixed oxides over the desired $PrInO_3$. Further, it must be pointed out that while the CA-assisted synthetic route is reported to yield single-phase products, our screening of 17 metal oxides resulted in variability, meaning that phase purity depends on optimized conditions, as some XRD patterns had small impurity peaks. However, by comparing the XRD patterns of powders synthesized with and without CA for $CaTiO_3$, $SrTiO_3$, $CaZrO_3$, and $MgTiO_3$, Figure S2 (a-d), it is unveiled that CA enhances the formation of the desired phase. Such an influence justified its ability to stabilize metal-citrate complexes, permit a homogeneous dispersion of cations, and suppress undesired phases.

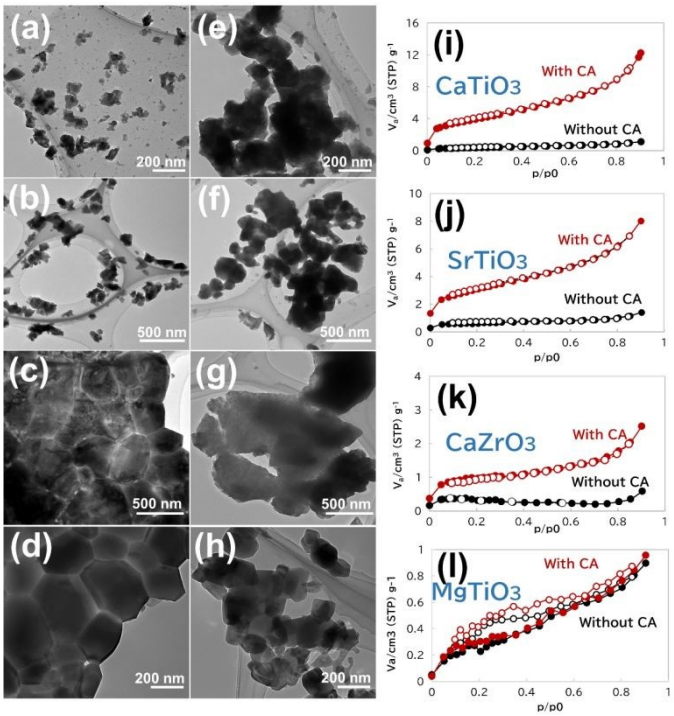

Figure 2: TEM images of $CaTiO_3$, $SrTiO_3$, $CaZrO_3$, and $MgTiO_3$ synthesized with CA (a–d) and without CA (e–h), along with their corresponding N_2 adsorption-desorption isotherms (i–l).

Transmission electron microscopy (TEM) images further revealed the significant morphological differences induced by CA, Figure 2. For $CaTiO_3$ and $SrTiO_3$, samples prepared with CA display small, well-dispersed nanoparticles, confirming that CA is highly effective at inhibiting particles' agglomeration and facilitating uniform dispersion, Figures 2a and b, respectively. Without CA, however, there is significant agglomeration, resulting in large clusters of particles exposing less surface area, Figures 2e and f, respectively. In $CaZrO_3$ and $MgTiO_3$, CA is credited for the formation of hexagonal-like, well-shaped particles with well-defined boundaries, indicative of controlled nucleation and growth with homogeneously sized particles, Figures 2c and d, respectively. In the absence of CA, the materials exhibit more irregular and aggregated structures with ill-defined particle morphology, Figure 2g and h, respectively. Thus, the influence of CA on the final morphology—whether forming well-dispersed nanoparticles or a well-organized structure—is largely governed by the elemental composition of the system. The choice of metal composition dictates how CA directs the nucleation, growth, and final organization of the material. Brunauer–Emmett–Teller (BET) surface area analysis further confirms that the impact of CA addition remains evident even after its complete removal through calcination at 1000°C. The addition of CA during the synthesis increases the surface area of the perovskites due to improved particle dispersion and controlled growth with the

chelating nature of CA, but the extent of CA influence varies with the elemental composition, Figure 2i-l. The BET surface area and the pore volume of the four perovskites are summarized in Table S3**.**

3.2 Photocatalyst performance evaluation results

Figure 3 illustrates the photocatalytic activities and the number of literature reports of 16 different ABO3-type photocatalysts, along with a mixed oxide that did not become a single ABO3-type structure. The raw decay data of MB and each material is shown in Figure S3 and S4. As shown in Figure S5, compared to the light irradiating condition, a negligible decrease is caused by either adsorption or dark performance within the 24-hour period. The perovskites are arranged in descending order with respect to their activities. The overlay in Figure 3 also includes and shows the number of previous reports on photocatalytic MB degradation for these perovskites, obtained through a Web of Science search conducted on August 28, 2024, using the keywords 'photocatalyst,' 'methylene blue,' and the respective perovskites' names.

In Figure 3, all the samples are shown to catalyze MB decomposition more efficiently than photolysis. Among the samples, the reaction rates of $CaTiO_3$ and $BaCeO_3$ are notably higher than the other materials, including the most studied photocatalyst, $SrTiO_3$. When comparing alkali earth metal-Ti-oxide photocatalysts, the observed trend follows $CaTiO_3$ > $SrTiO_3$ ≈ $BaTiO_3$ > $MgTiO_3$, which mostly corresponds to their periods in the periodic table, except for $MgTiO_3$. Vijayakumar et al. reported that $MgTiO_3$ exhibited lower performance than $CaTiO_3$ in Rhodamine B degradation.[36] They attributed this to the stronger Mg–O bonds in $MgTiO_3$, which make the bond cleavage and subsequent generation of reactive electron/hole pairs and radicals more difficult, while the weaker Ca–O bonds in $CaTiO_3$ facilitate these processes. Additionally, the aggregated nature of $MgTiO_3$ further reduced its photocatalytic activity. Similarly, various local factors govern photocatalytic performance. Investigating each of these factors in detail would be an extensive task beyond the scope of this study. However, while many efforts have been made to explore such individual local factors, this study aims to redefine a broader perspective by comparing a diverse range of materials under identical conditions.

A comparison between the performance ranking and the number of literature reports reveals that the high-performing materials identified in this study are not necessarily the ones most frequently investigated. Although it is generally expected that materials exhibiting superior performance would attract more research attention, discrepancies can possibly arise because previous studies often employ varied synthesis conditions (e.g., temperature, atmosphere, methods, and the presence of optimized co-catalysts). Judging from the small number of publications, however, it is more probable that the materials have not been explored in sufficient depth. In practice, many investigations tend to follow existing literature when selecting materials, which can lead the field to concentrate on similar material systems and potentially become trapped in local optima. In contrast, our study employs a uniform synthesis condition—calcination at 1000 °C in ambient air—to ensure a fair comparison of the intrinsic catalytic abilities of bare perovskites. This approach not only provides valuable reference data on materials that have yet to be fully optimized but also opens new opportunities for new materials discovery.

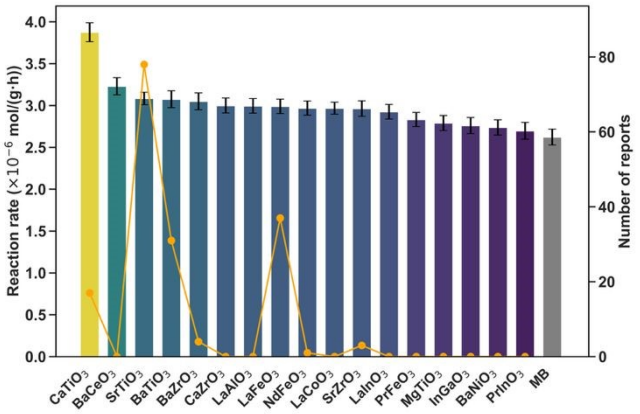

Figure 3: Overlaid figures show the photocatalytic performance and the number of reports for 16 ABO_3-type photocatalysts. The colored bars correspond to the reaction rate constants on the left axis, while the white line represents the number of reports on the right axis.

Note: The number of reports was determined through a Web of Science search conducted on August 28th, 2024, using the keywords 'photocatalyst,' 'methylene blue,' and the respective semiconductor names.

It should be accounted that MB itself degrades under Xe lamp irradiation even without a photocatalyst, as shown in Figure 3 and Figure S2. This is a critical point, since common experimental procedures involve the use of optical filters to specifically exclude the absorption band of MB itself, thereby biasing the evaluation of photocatalytic activity. A standard procedure used is irradiating with black light (which is purely UV light) to obtain quantum yields and extrapolating over photocatalytic activity under sunlight. But photocatalytic performance is known to be wavelength-dependent, and such results can be perilous to extrapolate further without further experimentation. Accordingly, in this research, photocatalytic MB degradation with and without the photocatalyst was compared under circumstances where photolysis of MB is feasible, without using cutoff filters, to ensure a fair evaluation of the photocatalytic performance.

Next, the general factors influencing photocatalytic performance are discussed based on unbiased experimental results, not influenced by previous research trends. Figure 4 shows the relationship between material properties and performance, with multiple physical properties from the Materials Project database reduced to two dimensions using principal component analysis (PCA). In the PCA analysis, the descriptor representing stability, “formation energy per atom”, and the descriptor representing the electronic structure, “vbm (valence band maximum)”, and “cbm (conduction band minimum)” were chosen. It can be observed that cbm are nearly

View Article Online
DOI: 10.1039/D5MA00345H

perpendicular to the reaction rate vector, while formation_energy_per_atom are almost aligned in the opposite direction of the reaction rate vector. The perpendicular vectors suggest that these properties contribute little to performance, indicating that cbm has minimal influence on photocatalytic performance. On the other hand, the angle between vbm and the reaction rate vector is slightly greater than 90°, implying that a lower vbm contributes to an enhanced reaction rate. Moreover, the formation_energy_per_atom, which points in the opposite direction to the reaction rate, is a descriptor related to stability—indicating that higher stability is associated with an increased reaction rate. These results suggest that descriptors based on elements or ions, which directly provide reaction sites, may capture aspects of photocatalytic performance that are not fully explained by conventional electronic structure parameters like band edge positions. Traditionally, a higher cbm and a vbm are considered desirable for photocatalysis, as they correspond to stronger reduction and oxidation potentials, respectively. However, the present analysis indicates that these thermodynamic requirements alone may be insufficient to explain the observed activity.

Indeed, even if the cbm is high enough to thermodynamically enable a reduction reaction, sufficient photocatalytic performance cannot be achieved unless two additional kinetic conditions are met: (i) effective supply of photogenerated carriers to the surface through light absorption, exciton separation, and carrier diffusion; and (ii) fast surface reactions that overcome activation barriers.[37] This implies that photocatalytic activity is determined not only by the feasibility of the reaction (as dictated by band positions), but also by the ability to sustain carrier transport and surface reaction kinetics. In this context, the observed relevance of formation energy per atom—while unlikely to directly represent these kinetic factors—may reflect underlying material characteristics that influence them. Consequently, this result highlights the limitations of evaluating photocatalytic activity solely based on band structure, and emphasizes the need to consider kinetic descriptors that are often overlooked in conventional analysis.

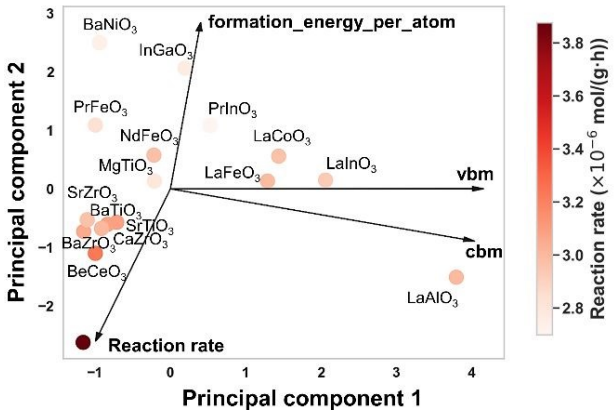

Figure 4: Correlation between material properties and performance.

Note: Multiple physical properties from the Materials Project database were reduced to two dimensions using PCA. The arrows represent vectors from the original dimensions displayed in 2D, with samples scattered on the 2D plane. The color of the samples indicates performance, with darker red representing higher performance.

4. Conclusions

This work describes an HTE approach that tackles the labor-intensive tasks associated with catalyst preparation by employing a citric acid-assisted synthesis route. One of the key strengths of this methodology is its versatility, which makes it possible to parallelly synthesize a large number of metal oxides within a short time frame. The approach is targeted not only at the parallelization of the synthesis technique but also at the screening of a wide range of perovskite compositions regarding photocatalytic performance. Such a systematic investigation, including less commonly studied perovskites, can serve for novel high-performance photocatalysts discovery, where $CaTiO_3$ stands out and shows promising performance for photocatalytic material. Furthermore, principal component analysis based on a dataset unified in synthesis and evaluation methods suggests the limited influence of band structure on performance and highlights the greater relevance of element or ion-based descriptors. This systematic workflow can accelerate the identification of effective photocatalysts and anticipate the necessary insight into the structure-property relationship governing photocatalytic performance.

Conflicts of interest

There are no conflicts to declare.

Data availability

The data supporting this article have been included as part of the ESI.†

Funding

This study was partly supported by Toyota Motor Corporation. We also appreciate the financial support from JSPS Kakenhi (Grant Number 24KJ1201).

References

1 S. Ali, J. Abdul Nasir, R. Nasir Dara and Z. Rehman, *Inorg Chem Commun*, 2022, **145**, 110011.

2 C. Sun, J. A. Alonso and J. Bian, *Adv Energy Mater*, 2021, **11**, 2000459.

3 L.-P. Yuan, W.-J. Jiang, X.-L. Liu, Y.-H. He, C. He, T. Tang, J. Zhang and J.-S. Hu, *ACS Catal*, 2020, **10**, 13227–13235.

4 C. An, Y. Zhang, H. Guo and Y. Wang, *Nanoscale Adv*, 2019, **1**, 4644–4658.

5 J. Kim, W. Ko, J. M. Yoo, V. K. Paidi, H. Y. Jang, M. Shepit, J. Lee, H. Chang, H. S. Lee, J. Jo, B. H. Kim, S. Cho, J. van Lierop, D. Kim, K. Lee, S. Back, Y. Sung and T. Hyeon, *Advanced Materials*, 2022, **34**, 2107868.

6 J. S. Manser, J. A. Christians and P. V. Kamat, *Chem Rev*, 2016, **116**, 12956–13008.

7 H. Mai, D. Chen, Y. Tachibana, H. Suzuki, R. Abe and R. A. Caruso, *Chem Soc Rev*, 2021, **50**, 13692–13729.

8 K. S. Schanze, P. V. Kamat, P. Yang and J. Bisquert, *ACS Energy Lett*, 2020, **5**, 2602–2604.

9 F. Temerov, Y. Baghdadi, E. Rattner and S. Eslava, *ACS Appl Energy Mater*, 2022, **5**, 14605–14637.

10 A. Kumar, A. Kumar and V. Krishnan, *ACS Catal*, 2020, **10**, 10253–10315.

11 Z. Kalaycıoğlu, B. Özuğur Uysal, Ö. Pekcan and F. B. Erim, *ACS Omega*, 2023, **8**, 13004–13015.

12 K. Sathiyan, R. Bar-Ziv, O. Mendelson and T. Zidki, *Mater Res Bull*, 2020, **126**, 110842.

13 A. Negash, S. Mohammed, H. D. Weldekirstos, A. D. Ambaye and M. Gashu, *Sci Rep*, 2023, **13**, 22234.

14 S. Xia, L. Zhang, G. Pan, P. Qian and Z. Ni, *Phys. Chem. Chem. Phys.*, 2015, **17**, 5345–5351.

15 C. Yang, W. Dong, G. Cui, Y. Zhao, X. Shi, X. Xia, B. Tang and W. Wang, *Sci Rep*, 2017, **7**, 3973.

16 J. Fito, M. Abewaa, A. Mengistu, K. Angassa, A. D. Ambaye, W. Moyo and T. Nkambule, *Sci Rep*, 2023, **13**, 5427.

17 J. Wang, Y. Tan, H. Yang, L. Zhan, G. Sun and L. Luo, *Sci Rep*, 2023, **13**, 21174.

18 Y.-Y. Lau, Y.-S. Wong, T.-T. Teng, N. Morad, M. Rafatullah and S.-A. Ong, *RSC Adv*, 2015, **5**, 34206–34215.

19 I. Yahiaoui, F. Aissani-Benissad, K. Madi, N. Benmehdi, F. Fourcade and A. Amrane, *Ind Eng Chem Res*, 2013, **52**, 14743–14751.

20 E. H. Khader, S. A. Muslim, N. M. C. Saady, N. S. Ali, I. K. Salih, T. J. Mohammed, T. M. Albayati and S. Zendehboudi, *Desalination Water Treat*, 2024, **318**, 100384.

21 D. Ma, H. Yi, C. Lai, X. Liu, X. Huo, Z. An, L. Li, Y. Fu, B. Li, M. Zhang, L. Qin, S. Liu and L. Yang, *Chemosphere*, 2021, **275**, 130104.

22 P. K. Pandis, C. Kalogirou, E. Kanellou, C. Vaitsis, M. G. Savvidou, G. Sourkouni, A. A. Zorpas and C. Argirusis, *ChemEngineering*, 2022, **6**, 8.

23 V. Shinde, P. Tanwade, T. Katayama, A. Furube, B. Sathe and P. Koinkar, *Surfaces and Interfaces*, 2024, **46**, 104067.

24 M. A. Ashwini, S. Sagadevan, I. Fatimah, S. Paiman, S. Upadhyay, S. Garg and M. R. Johan, *J Alloys Compd*, 2025, **1025**, 180296.

25 C. J. Bartel, C. Sutton, B. R. Goldsmith, R. Ouyang, C. B. Musgrave, L. M. Ghiringhelli and M. Scheffler, *Sci Adv*, 2019, **5**, eaav0693.

26 K. Yanagiyama, K. Takimoto, S. Dinh Le, N. Nu Thanh Ton and T. Taniike, *Environmental Pollution*, 2024, **342**, 122974.

27 P. Chammingkwan, M. Terano and T. Taniike, *ACS Comb Sci*, 2017, **19**, 331–342.

28 T. N. Nguyen, T. T. P. Nhat, K. Takimoto, A. Thakur, S. Nishimura, J. Ohyama, I. Miyazato, L. Takahashi, J. Fujima, K. Takahashi and T. Taniike, *ACS Catal*, 2020, **10**, 921–932.

29 T. P. Jayakumar, S. P. Suresh Babu, T. N. Nguyen, S. D. Le, R. P. Manchan, P. Phulkerd, P.

View Article Online
DOI: 10.1039/D5MA00345H

Chammingkwan and T. Taniike, *Appl Catal A Gen*, 2023, **666**, 119427.

30 Y. Guo, W. Sato, K. Shoyama, H. Halim, Y. Itabashi, R. Shang and E. Nakamura, *J Am Chem Soc*, 2017, **139**, 9598–9604.

31 M. Li, M. Feng, C. Guo, S. Qiu, L. Zhang, D. Zhao, H. Guo, K. Zhang and F. Wang, *ACS Appl Mater Interfaces*, 2023, **15**, 16942–16952.

32 G. Dantelle, S. Beauquis, R. Le Dantec, V. Monnier, C. Galez and Y. Mugnier, *Small*, 2022, **18**, 2200992.

33 Z. Zhang, Q. Gao, Y. Liu, C. Zhou, M. Zhi, Z. Hong, F. Zhang and B. Liu, *RSC Adv*, 2015, **5**, 84280–84283.

34 A. Jain, S. P. Ong, G. Hautier, W. Chen, W. D. Richards, S. Dacek, S. Cholia, D. Gunter, D. Skinner, G. Ceder and K. A. Persson, *APL Mater*, 2013, **1**, 011002.

35 S. P. Ong, W. D. Richards, A. Jain, G. Hautier, M. Kocher, S. Cholia, D. Gunter, V. L. Chevrier, K. A. Persson and G. Ceder, *Comput Mater Sci*, 2013, **68**, 314–319.

36 N. Vijayakumar, S. K. Venkatraman, S. Imthiaz, E. A. Drweesh, M. M. Elnagar, S. Koppala and S. Swamiappan, *Sci Rep*, 2023, **13**, 3615.

37 Y. Cho, K. Yanagiyama, P. Mukherjee, P. Phulkerd, K. Sathiyan, E. Sawade, T. Wada and T. Taniike, *J Mater Chem A*, 2025.DOI:10.1039/D5TA00415B.

View Article Online
DOI: 10.1039/D5MA00345H

The data supporting this article have been included as part of the ESI. †